POLITECNICO DI TORINO
Repository ISTITUZIONALE

Investigating the solute concentration in capillary-fed vapor generators: A heat and mass transfer study

Original
Investigating the solute concentration in capillary-fed vapor generators: A heat and mass transfer study / Meo, R.R., Provenzano, M., Morciano, M.. - In: INTERNATIONAL COMMUNICATIONS IN HEAT AND MASS TRANSFER. - ISSN 0735-1933. - ELETTRONICO. - 148:(2023). [10.1016/j.icheatmasstransfer.2023.106998]

Availability:
This version is available at: 11583/2981697 since: 2023-09-06T08:39:59Z

Publisher:
Elsevier

Published
DOI:10.1016/j.icheatmasstransfer.2023.106998

Terms of use:

This article is made available under terms and conditions as specified in the corresponding bibliographic description in the repository

Publisher copyright

(Article begins on next page)

17 September 2026

International Communications in Heat and Mass Transfer 148 (2023) 106998

Contents lists available at ScienceDirect

International Communications in Heat and Mass Transfer

journal homepage: www.elsevier.com/locate/ichmt

Investigating the solute concentration in capillary-fed vapor generators: A heat and mass transfer study

Roberto Raffaele Meo [a,1], Marina Provenzano [a], Matteo Morciano [a,b,*,1]

[a] Department of Energy, Politecnico di Torino, Corso Duca degli Abruzzi 24, 10129 Torino, Italy
[b] Clean Water Center, Politecnico di Torino, Corso Duca degli Abruzzi 24, 10129 Torino, Italy

ARTICLE INFO

Keywords:
Solute transport
Interfacial evaporation
Water treatment
Vapor generation
Passive desalination
Sustainability

ABSTRACT

Interfacial passive thermal evaporation is currently attracting considerable interest from the scientific community in light of its zero consumption of fossil fuels and its important implications in the field of sustainable water purification. However, very few works comprehensively address the crystalline solute deposition issue, which is the Achilles' heel of this process. Here, we propose a numerical analysis of the solute concentration in the device to quantify the saturation times together with the operating condition ranges to act within to prevent crystallization. A simplified analytical approach is then proposed, which provides accurate information at the most critical and design-wise interesting point. The phenomenon of solute accumulation is revealed to exhibit an exponential trend over time, as determined by a time constant Γ. Interestingly, the saturation times can be easily estimated as 2.3 Γ. In detail, the saturation time evaluated with the analytical model is estimated as 2 h, in the case of a 2-meter length device, which is approximately 5% less than the numerically estimated value. In conclusion, this study aims at exploring, quantifying and discussing the limitations of wick-based media used to design solar/thermal interfacial passive evaporation devices, from the perspective of solute accumulation.

1. Introduction

In recent years, passive interfacial thermal (e.g. solar-powered) evaporation [1] has received considerable interest from the scientific community, as a result of its significant implications for sustainable water purification and desalination, especially in isolated and impoverished off-grid areas. [2–5] This process is characterized by low cost, reduced environmental impact and high solar-to-vapor conversion efficiency. [1,6,7] However, technologies based on it are still not ready for practical application and their deployment and widespread adoption currently represent a great challenge. [8,9] The aforementioned strengths are indeed accomplished at the expense of the lack of energy-consuming active parts, thus exploiting the inherently limited passive transport of aqueous solutions in more confined pathways. [4,7,10,11] Indeed, localization of heat, which is mainly responsible for the high solar-to-vapor conversion, requires reduced thicknesses of the photothermal element, the latter typically being a low-cost porous material through which water flows driven by capillary action. Therefore, passive interfacial thermal evaporation suffers two major issues, i.e., reduced scalability [8] due to the capillary limit, which was extensively investigated and discussed in our recent work [9], and the conversion efficiency decay over time because of the crystalline solute deposition within the photothermal component. [8,12] In detail, during evaporation, crystalline solute accumulates on the surface of the evaporator, clogging the water supply pathway, and thereby reducing the capillary effect, lowering vapor pressure and hindering light absorption. The concurrence of all these phenomena suppresses further water vapor generation compromising the stability of long-term functioning [2].

The state-of-art counts several works, predominantly experimental, where a variety of representative mitigation strategies have been proposed with the aim of developing anti-clogging photothermal structures able to sustain high efficiency over time, while preventing crystalline solute deposition. As reported by Sheng and co-workers [2] and Li and co-workers [11] in their comprehensive review papers, the proposed strategies are mainly based on mechanical crystalline solute removal by manual action or forced flushing [3], which does not guarantee continuous production and is not suitable for large-scale production [13]. Alternatively, gravity and surface tension-driven [14,15] enhanced fluid convection and shielding effect have been obtained by means of chemical surface engineering [16–19]. This approach relies on

* Corresponding author at: Department of Energy, Politecnico di Torino, Corso Duca degli Abruzzi 24, 10129 Torino, Italy.
E-mail address: matteo.morciano@polito.it (M. Morciano).
[1] these two authors contributed equally to this work

https://doi.org/10.1016/j.icheatmasstransfer.2023.106998
Received 7 June 2023; Received in revised form 31 July 2023; Accepted 16 August 2023
Available online 30 August 2023
0735-1933/© 2023 The Authors. Published by Elsevier Ltd. This is an open access article under the CC BY license (http://creativecommons.org/licenses/by/4.0/).

the use of ad hoc hydrophobic layers or hydrophobic–hydrophilic Janus structures [17,18], both designed to keep solute crystallisation away from the evaporation area.

However, to the best of our knowledge, very few works propose a comprehensive and quantitative study of the species mass transfer in photothermal materials used for interfacial solar/thermal evaporation. This study is devoted to investigate and predict, through a numerical and analytical approach, the local and time-dependent solute concentration in the wick-based porous photothermal component. In detail, time-dependent sensitivity analyses were performed with the theoretical model under varying operating conditions to comprehend the effect of different parameters, such as absorbed thermal energy (and accordingly evaporation rate) and device geometry, on the solute concentration along the device and on the characteristic saturation times. The latter indicate the attainment of the saturation concentration at the most critical point of the device. It is worth noting that, the proposed dynamic model considers the velocity reduction of the propagating front due to the interfacial evaporation. The mathematical function describing the local velocity, and thus the evaporation rate, was derived in our previous work. [9] Additionally, a simplified analytical model, based on physical considerations and numerical results, is proposed to determine in a preliminary and straightforward way the design domain of the device within which to operate safely.

Finally, we believe that this approach could i) assist the design steps of the wick-based evaporator to ensure as high and stable the water yield as possible, without reaching crystalline solute deposition, and ii) encourage the conceptualization of structures able to spatially isolate solute crystallization. This last attractive solution was proposed in several recent articles [20–23] with the aim of favouring the recovery of the solid waste, the latter being the main objective of zero liquid discharge (ZLD) treatments characterised by brine disposal with reduced impact on the marine ecosystem [2].

2. Theoretical background and methods

2.1. Passive interfacial thermal evaporation

In Fig. 1, half of the wick-based porous medium saturated with aqueous solution is schematically represented together with the process of thermal energy absorption, interfacial evaporation, and resulting solute concentration. The water to be treated enters from the left side at a fixed concentration, while the right side represents the center of the device (i.e., the symmetry axis) and thus the most critical point for the solute rejection. Here, without losing generality, seawater (i.e., exhibiting 1:1 ratio of sodium and chloride ions) is considered as an aqueous solution absorbed and confined by the wick-based porous layer with photothermal properties.

As discussed by Meo and co-workers in Ref. [9], the velocity reduction of the propagating front of the water flow due to interfacial evaporation can be obtained by applying the first law of thermodynamics to the fixed Eulerian control volume shown in Fig. 1 (i.e., half of the symmetric horizontal evaporator) and the conservation of mass to a generic infinitesimal volume, while assuming constant temperature along the evaporator and steady-state conditions. This represents a limiting case where the flow rate is at most overestimated allowing for conservative results in terms of solute accumulation and thus saturation times. Therefore, considering a one-dimensional approximation distributed model, we get:

$$\Delta\dot{x} = \frac{\dot{m}_{evap}x}{\rho s\varepsilon} = \frac{\frac{q_{in}x}{h_{gl}(T)-c_{p,w}T}}{\rho s\varepsilon} \tag{1}$$

$$= \frac{1}{\rho\varepsilon}\frac{\frac{q_{in}}{s}}{h_{gl}(T)-c_{p,w}T}x$$

where s and ε are the thickness and porosity of the wick-based evaporator, respectively. The porosity is defined as the ratio of the volume of the voids or pore space divided by the total volume of the porous medium. Then, ρ the density of the aqueous solution; x the fixed local reference coordinate with origin at the entrance section (left side of the wick-based evaporator) and $\dot{m}_{evap}$ the specific evaporating mass flow rate expressed in [kg m^{-2} s^{-1}]; q_{in} the specific incoming thermal energy expressed in [W m^{-2}]; h_{gl} the enthalpy of vaporization at a certain temperature T and $c_{p,w}$ the specific heat of water. It is worth noting that extensive details on the validity of the near-uniform temperature hypothesis along the evaporator were reported in our previous work (see Ref. [9]), where the expression for $\dot{m}_{evap}$ was obtained by considering its dependence on a mass transfer coefficient, due to partial pressure gradient, and the partial pressure driving force. Moreover, x ranges between 0 and L, with $L < L_{max}$ being L_{max} the maximum critical distance reachable by the fluid front in the porous material without undergoing dry-out phenomena. Findings on L_{max} under varying operating conditions were discussed in Ref. [9], where a fluid dynamic model was

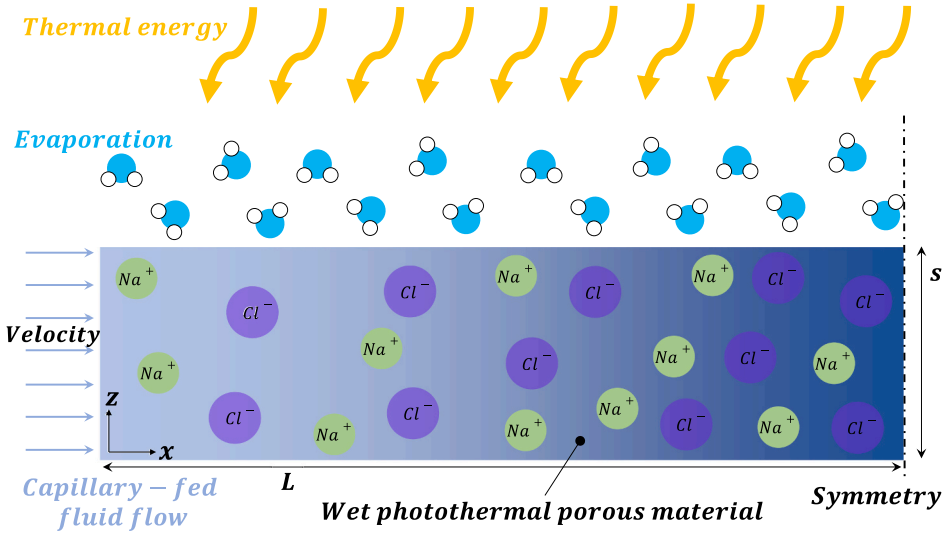

Fig. 1. Illustrative picture of the phenomenon of passive interfacial thermal evaporation. Here, the aqueous solution confined by a wick-based evaporator of thickness s is heated up by the incoming thermal energy and a continuous evaporation process takes place, together with concentration of the solute. Here, without losing generality, seawater (i.e., exhibiting 1:1 ratio of sodium and chloride ions) is considered.

developed. The latter was comprehensive of the local acceleration (the inertial term) of the fluid; the capillary pressure, which depends on the surface tension, the contact angle, the density of the fluid and the radius of the porous material; the eventual hydrostatic pressure, which depends on the gravity and the height; the dynamic pressure, which depends on the square of the velocity of the fluid; and the viscous losses (based on the Darcy's law) in the capillary, which depend on the viscosity of the fluid, the density, the radius of the porous material, the coordinate and the velocity of the fluid. Derivation details are reported and extensively discussed in Ref. [9].

2.2. Advection–diffusion equation for solute transport

Applying the continuity equation to a fixed Eulerian control volume Ω, which here represents the aqueous solution confined in the porous medium (see Fig. 1), we get:

$$\frac{d}{dt}\int_{\Omega}\rho\varepsilon a d\Omega = -\oint_{\partial\Omega}\left(\mathbf{\Phi}_{diffusive}+\mathbf{\Phi}_{advective}\right)\cdot\mathbf{n}d\Sigma \tag{2}$$

where a represents the solute concentration. On the right-hand side, the diffusive $\mathbf{\Phi}_{diffusive}$ and advective $\mathbf{\Phi}_{advective}$ terms are reported. The diffusive term can be expressed as $\mathbf{\Phi}_{diffusive} = -\frac{\varepsilon D_{Fick}}{\tau}\rho\nabla a$, where D_{Fick} is the diffusion coefficient of solute in water and τ the tortuosity of the porous medium, which accounts for the difference between the effective average length of the flow paths and the length of the porous medium. The latter parameter can be evaluated by using the Mackie-Maeres equation [24,25], namely $\tau = \frac{(2-\varepsilon)^2}{\varepsilon}$. Then, the advective term is $\mathbf{\Phi}_{advective} = \dot{\mathbf{m}}a$, where $\dot{\mathbf{m}}$ is the specific mass flow rate vector evaluated in [kg m^{-2} s^{-1}]. In detail, applying the conservation of mass to a generic infinitesimal volume of the evaporator shown in Fig. 1 we get $\frac{d\dot{m}}{dx} = -\frac{\dot{m}_{evap}}{s}$. Thus, the term on the left-hand side of Eq. (2) is the total change of solute mass in the control volume Ω, whilst the term on the right-hand side represents the mass which flows through the borders, that is the scalar product between the generic mass flow vector and the local normal versor $\mathbf{n}$ to the border $\partial\Omega$, being $d\Sigma$ an infinitesimal portion of the border. The versor is defined positive if outgoing. Substituting into the general equation and considering that the boundary Ω has been assumed fixed over time, the previous equation can be rewritten as:

$$\int_{\Omega}\frac{\partial}{\partial t}(\rho\varepsilon a)d\Omega = -\oint_{\partial\Omega}\frac{\varepsilon D_{Fick}}{\tau}\rho\nabla a\cdot\mathbf{n}d\Sigma + -\oint_{\partial\Omega}\dot{\mathbf{m}}a\cdot\mathbf{n}d\Sigma \tag{3}$$

Exploiting the Gauss's theorem, the surface integrals can be replaced by the volume integrals:

$$\int_{\Omega}\frac{\partial}{\partial t}(\rho\varepsilon a)d\Omega = \int_{\Omega}\nabla\cdot\left(\frac{\varepsilon D_{Fick}}{\tau}\rho\nabla a\right)d\Omega + -\int_{\Omega}\nabla\cdot(\dot{\mathbf{m}}a)d\Omega \tag{4}$$

Since the derived law is valid for any volume Ω, small at will, it is possible to write:

$$\frac{\partial}{\partial t}(\rho\varepsilon a) = \nabla\cdot\left(\frac{\varepsilon D_{Fick}}{\tau}\rho\nabla a\right) - \nabla\cdot(\dot{\mathbf{m}}a) \tag{5}$$

Assuming constant the diffusion coefficient D_{Fick}, the porosity ε, the tortuosity τ and the density ρ, and considering a one-dimensional approximation distributed model, we get:

$$\rho\varepsilon\frac{\partial a}{\partial t} = \frac{\varepsilon D_{Fick}}{\tau}\rho\frac{\partial^2 a}{\partial x^2} - \varepsilon\rho\frac{\partial(\dot{x}a)}{\partial x} \tag{6}$$

where the specific (namely, per unit of cross section) mass flow rate along x was considered equal to $\dot{m} = \varepsilon\rho\dot{x}$. Furthermore, the wicking velocity of the fluid along the evaporator, based on Eq. (1), may be expressed by the following equation, which then recovers the zero velocity value at the axis of symmetry (i.e., $x = L$):

$$\dot{x} = \frac{1}{\rho\varepsilon}\frac{\frac{q_{in}}{s}}{h_{gl}(T)-c_{p,w}T}L\left(1-\frac{x}{L}\right) \tag{7}$$

Then, it is interesting to generalize the problem by adimensionalizing the x variable. Thus, the previous Eq. is written in dimensionless form, considering $\tilde{x} = \frac{x}{L}$, with $L < L_{max}$:

$$\rho\varepsilon\frac{\partial a}{\partial t} = \frac{\frac{\varepsilon D_{Fick}}{\tau}\rho}{L^2}\frac{\partial^2 a}{\partial\tilde{x}^2} - \frac{\frac{q_{in}}{s}}{h_{gl}(T)-c_{p,w}T}\frac{\partial[(1-\tilde{x})a]}{\partial\tilde{x}} \tag{8}$$

Then, we can discretize in the space replacing the derivatives with finite differences, choosing $\Delta\tilde{x}$ such that $\Delta\tilde{x} < \frac{2}{Pe}$, to avoid spurious oscillations and instabilities. Up-winding scheme is required to mitigate possible numerical instabilities being a diffusive-advective problem. At the generic node of the discretization of index j, the following equation can be written:

$$\rho\varepsilon\dot{a}_j = \frac{\frac{\varepsilon D_{Fick}}{\tau}\rho}{L^2}\frac{a_{j+1}-2a_j+a_{j-1}}{\Delta\tilde{x}^2} + \tag{9}$$

$$-\frac{\frac{q_{in}}{s}}{h_{gl}(T)-c_{p,w}T}\frac{(1-\tilde{x}_j)a_j-(1-\tilde{x}_{j-1})a_{j-1}}{\Delta\tilde{x}}$$

Then, to compact the equation, we resort two parameters $\alpha = \frac{\frac{q_{in}}{s}}{h_{gl}(T)-c_{p,w}T}$ and $\beta = \frac{\frac{\varepsilon D_{Fick}}{\tau}\rho}{L^2}$, obtaining:

$$\rho\varepsilon\dot{a}_j - \left[\frac{\alpha(1-\tilde{x}_{j-1})}{\Delta\tilde{x}}+\frac{\beta}{(\Delta\tilde{x})^2}\right]a_{j-1} + \tag{10}$$

$$+\left[\frac{\alpha(1-\tilde{x}_j)}{\Delta\tilde{x}}+\frac{2\beta}{(\Delta\tilde{x})^2}\right]a_j - \frac{\beta}{(\Delta\tilde{x})^2}a_{j+1} = 0$$

The problem under investigation can be encapsulated in matrix notation as $\rho\varepsilon\mathbf{I}\dot{a} + \mathbf{A}a = b$, where I denotes the identity matrix, A characterizes the problem's stiffness matrix, and b symbolizes the forcing term. The matrix A has a tridiagonal structure of order N, where N + 1 corresponds to the total number of nodes in the discretization process intended to determine the unknown solute concentration value. The coefficients in the initial and final rows of the matrix are defined by applying specific boundary conditions. A Dirichlet condition is enforced at $\tilde{x} = 0$, reflecting a fixed concentration at the inlet of the wick-based evaporator due to the proximal sea basin. This is mathematically represented as $a_0(\tilde{x} = 0, t) = a_{sea}$ and serves as a forcing term. In its absence, b would simply be a vector filled exclusively with zeros (as derived from Eq. (10)). On the other hand, a Neumann condition is applied at $\tilde{x} = 1$. This is due to symmetry conditions at the center of the device, which dictate that the diffusive flux of solute must be null. These boundary conditions collectively account for the distinct characteristics inherent to the physical problem. The imposition of the Dirichlet condition requires a consequent revision of the b term:

$$b_1 = \left[\frac{\alpha(1-\tilde{x}_0)}{\Delta\tilde{x}}+\frac{\beta}{(\Delta\tilde{x})^2}\right]a_{sea} \tag{11}$$

To comply with the Neumann boundary condition $\frac{\partial a}{\partial\tilde{x}}(\tilde{x} = 1, t) = 0$, a centered incremental ratio is employed to approximate the first derivative. This yields the subsequent result:

$$\rho\varepsilon\dot{a}_N - \left[\frac{\alpha(1-\tilde{x}_{N-1})}{\Delta\tilde{x}}+\frac{2\beta}{(\Delta\tilde{x})^2}\right]a_{N-1} + \tag{12}$$

$$+\left[\frac{\alpha(1-\tilde{x}_N)}{\Delta\tilde{x}}+\frac{2\beta}{(\Delta\tilde{x})^2}\right]a_N = 0$$

To accurately track the temporal evolution of the spatial distribution of solute concentration, it is necessary to set a high number N of discretization nodes. However, this approach leads to significant computational overhead. Therefore, to manage the computational demands, the problem was preconditioned by utilizing the incomplete LU factorization of the stiffness matrix, and the solution was then accomplished using the biconjugate gradient method.

2.3. Simplified analytical approach

The study of the phenomenon may be considerably simplified as convection turns out to be dominant, under the considered operating conditions. Indeed, typical values of the involved parameters, $D_{Fick,\ NaCl} \approx 1.99 \times 10^{-9}$ m^2 s^{-1}, $100 \leqslant q_{in} \leqslant 10000$ W m^{-2}, 1 mm $\leqslant s \leqslant$ 1 cm and 10 cm $\leqslant L \leqslant$ 1 m lead to very high Péclet numbers (i.e., $Pe = \frac{\alpha}{\beta}$). Thus, simplifying the following equation:

$$\rho\varepsilon\frac{\partial a}{\partial t} - \beta\frac{\partial^2 a}{\partial \widetilde{x}^2} + \alpha\frac{\partial[(1-\widetilde{x})a]}{\partial \widetilde{x}} = 0 \tag{13}$$

we get accordingly:

$$\frac{\partial a}{\partial t} + k\frac{\partial[(1-\widetilde{x})a]}{\partial \widetilde{x}} = 0 \tag{14}$$

where, $k = \frac{\alpha}{\rho\varepsilon}$. The partial derivative differential equation, solvable in explicit form, was solved with the help of Wolfram. [26] The differential equation solution is:

$$a(\widetilde{x},t) = -\frac{f\left(\frac{\ln(k-k\widetilde{x})}{k} + t\right)}{\widetilde{x}-1} \tag{15}$$

Then, by imposing the initial condition, i.e., $a(\forall\widetilde{x}, t = 0) = a_{sea}$, we can easily get:

$$f\left(\frac{\ln(k-k\widetilde{x})}{k}\right) = (1-\widetilde{x})a_{sea} \tag{16}$$

which can be rewritten as:

$$f\left(\frac{\ln(k-k\widetilde{x})}{k}\right) = \frac{e^{k\left(\frac{\ln(k-k\widetilde{x})}{k}\right)}}{k}a_{sea} \tag{17}$$

and thus:

$$a(\widetilde{x},t) = \frac{\frac{e^{k\left(\frac{\ln(k-k\widetilde{x})}{k}+t\right)}}{k}}{1-\widetilde{x}}a_{sea} = a_{sea}e^{kt} \tag{18}$$

The derivation of Eq. (18) intrinsically upholds the Neumann boundary condition, even without explicitly imposing boundary conditions. This streamlined approach is crucial during the design stage. While the Dirichlet condition at the inlet is bypassed to avoid an overconstrained analytical problem, it is noteworthy that the Neumann condition is satisfied at the most critical point of the device, from the perspective of solute accumulation. Specifically, Eq. (18) accurately predicts the solute concentration at this critical juncture after a specific time t, due to evaporation. Despite its simplicity, this model offers a remarkably precise estimation of the behavior near the critical point, underlining its significant utility in design considerations. Alternatively, the imposition of the Dirichlet boundary condition requires the dismissal of the initial condition, given their mutual exclusivity in this system. The decision between adopting the Dirichlet boundary condition or the initial condition is contingent upon the specific physical context under investigation. The subsequent expression is derived under the adherence to the Dirichlet condition, specifically, $a(\widetilde{x} = 0, \forall t) = a_{sea}$ from Eq. (15):

$$f\left(\frac{\ln(k)}{k} + t\right) = a_{sea} \tag{19}$$

which can be written as:

$$f\left(\frac{\ln(k)}{k} + t\right) = \frac{e^{\ln\left(k^{\frac{1}{k}}e^t\right)}}{k^{\frac{1}{k}e^t}}a_{sea} \tag{20}$$

which, yields:

$$a(\widetilde{x},t) = -\frac{\frac{e^{\ln\left(k^{\frac{1}{k}(1-\widetilde{x})}\widetilde{k}^{\frac{1}{k}}e^t\right)}}{k^{\frac{1}{k}(1-\widetilde{x})}\widetilde{k}^{\frac{1}{k}}e^t}a_{sea}}{\widetilde{x}-1} = \frac{a_{sea}}{1-\widetilde{x}} \tag{21}$$

The expression of a obtained with Eq. (21) approximates very well the numerical solution of the problem around the Dirichlet condition, but less faithfully at the center of the wick-based evaporator as it does not respect the Neumann condition, which imposes zero diffusive flux at the symmetry axis, i.e., $\frac{\partial a}{\partial t}|_{\widetilde{x}=1} = 0$. It is worth noting that Eq. (21) can also be derived by considering the simplified differential equation (see Eq. (14)) under steady-state conditions. This implies that the simplified solution, complying with the Dirichlet condition, aligns with the theoretical steady-state conditions, which, in practice, are unattainable due to the onset of crystallization.

3. Results

In Fig. 2, the time-dependent salt concentration a as function of the dimensionless variable $\widetilde{x}$ is represented. The wick-based evaporator length L assumes three different values, namely 1 cm, 10 cm and 1 m. Then, two different volumetric thermal energy fluxes are considered. In detail, in panel a) q_{in} and s are equal to 1000 W m^{-2} and 1 mm, respectively; whilst in panel b) q_{in} and s are equal to 700 W m^{-2} and 2 mm, respectively. Note that the Dirichelt boundary condition applied to the left side of the evaporator (see Fig. 1) results in a equal to 35 g L^{-1}, which is the salinity of the sea.

Comparing the results obtained, it was observed that only for values of L of the order of a centimetre (see blue dashed line in Fig. 2) or less, the diffusive term affects the salt concentration profile. Indeed, a smoother evolution of the salt concentration, with respect to the case where L is equal to 10 cm and 1 m (see orange and red dash-dot lines in Fig. 2, respectively), was obtained along with a reduction in the length of the end portion of the evaporator, i.e., where the concentration remains approximately constant as the $\widetilde{x}$-coordinate changes. This segment at constant concentration is significantly more pronounced for L= 10 cm and L= 1 m. However, values of $L \leqslant 1$ cm are scarcely interesting from an engineering standpoint due to essentially almost zero productivity. Furthermore, it was found that for L greater than 10 cm, the time evolution of the salt concentration in the evaporator is essentially unalterable. Then, comparing Fig. 2a), the pronounced effect that the $\frac{q_{in}}{s}$ factor plays on the salt concentration profile can be appreciated, other parameters being equal. Considering q_{in} equal to 1000 W m^{-2} and 1 mm thickness (see Fig. 2a), it emerges that after only about 40 min of operation, the concentration reaches values close to saturation (with $a_{sat} \approx 350$ g L^{-1} in case of sodium chloride) at the most critical points of the device, namely at $\widetilde{x} = 1$. A slight increase in thickness to 2 mm and a q_{in} equal to 700 W m^{-2} (see Fig. 2b), which corresponds to the peak value recorded in Turin in August (according to PVGIS software [27]), results in a significant decrease in the concentrations reached at the most critical points, again after 40 min of operation. In detail, in case of $L \geqslant 0.01$ m, the concentration drops from over 350 g L^{-1} to about 75 g L^{-1}. This highlights the crucial role of the choice of evaporator layer thickness.

As discussed in Section 2.3, the problem investigated may be significantly simplified over a wide range of main parameter values. In Fig. 3, the reciprocal of the Pe numbers of the salt concentration phenomenon are quantified and represented. The maximum value of $\frac{1}{Pe}$ is approximately 0.03, considering $L \geqslant 10$ cm, with the minimum $\frac{q_{in}}{s}$ value

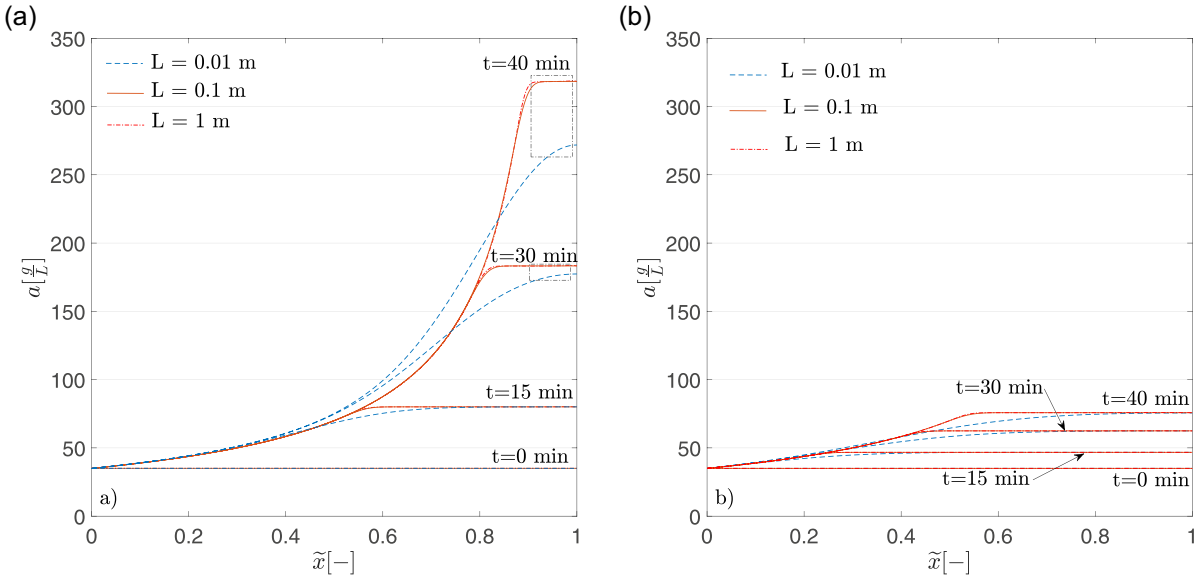

Fig. 2. Time-dependent salt concentration a as function of the dimensionless variable $\tilde{x}$. Blue dashed line, orange solid line and the red dash-dot line represent the numerical solution (see Eq. (10)) being L equal to 0.01 m, 0.1 m and 1 m, respectively. Moreover, in panel a) q_{in} and s are equal to 1000 W m^{-2} and 1 mm, respectively; whilst in panel b) q_{in} and s are equal to 700 W m^{-2} and 2 mm, respectively. The numerical solutions for t equal to 0, 15, 30 and 40 min are reported. Note that the Dirichelt boundary condition applied to the left side of the evaporator (see Fig. 1) is set at 35 g L^{-1}, which is the salinity of the sea.

(therefore minimizing the advective phenomenon). In the case of L equal to 5 cm, $\frac{1}{Pe}$ reaches a maximum of about 0.1, with the minimum $\frac{q_{in}}{s}$ value. Therefore, the diffusive phenomenon can be neglected in most cases, being a dominant advection problem.

In support of this, the weight of diffusion on salt accumulation in the wick-based evaporator can be determined. At the inlet of the wick-based evaporator two streams occur, namely the advective one, which introduces salt into the evaporator, and the diffusive one, which tends to expel salt. More specifically, we can write these contributions as:

$$\mathbf{\Phi}_{diffusive}\big|_{\tilde{x}=0} = -\frac{\varepsilon D_{Fick}}{L\tau}\rho\frac{\partial a}{\partial \tilde{x}}\bigg|_{\tilde{x}=0} = -\frac{\varepsilon D_{Fick}}{L\tau}\rho a_{sea} \tag{22}$$

$$\mathbf{\Phi}_{advective}\big|_{\tilde{x}=0} = \alpha L a_{sea} \tag{23}$$

where $\frac{\partial a}{\partial \tilde{x}}\big|_{\tilde{x}=0} \approx a_{sea}$. This approximation can be easily justified by looking

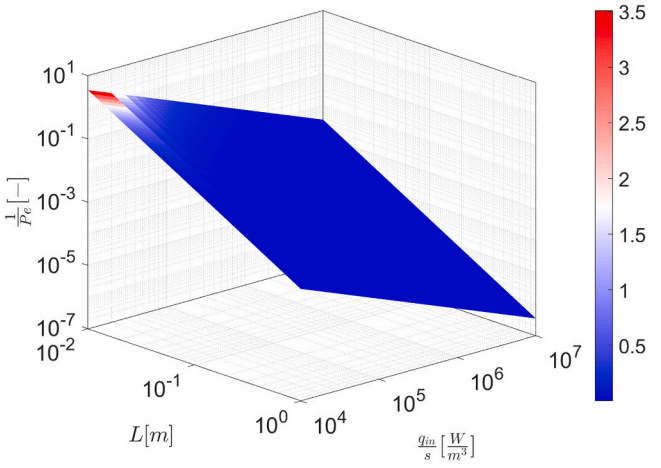

Fig. 3. The reciprocal of Péclet number $\frac{1}{Pe}$ as function of the volumetric absorption of thermal energy $\frac{q_{in}}{s}$ and the length of the wick-based evaporator L. In detail, the following ranges were considered: 100 ⩽q_{in}⩽10000 W m^{-2}, 1 mm ⩽s⩽1 cm and 1 cm ⩽L ⩽1 m.

at Fig. 4, where the results of Eq. (10) and those of Eq. (21) are found to be comparable in $\tilde{x} = 0$. The suitability of this choice was further verified by numerically deriving the result of Eq. (10). Thus, the ratio is:

$$r_{fluxes} = \frac{\left|\mathbf{\Phi}_{diffusive}\big|_{\tilde{x}=0}\right|}{\mathbf{\Phi}_{advective}\big|_{\tilde{x}=0}} = \frac{\frac{\varepsilon D_{Fick}}{\tau}\rho}{\alpha L^2} \approx 1,7\frac{s}{q_{in}L^2} \tag{24}$$

which is 0.017 at maximum for the considered application (q_{sun} = 100 W m^{-2}; s = 0.01 m and L = 0.1 m). Therefore the salt intake by convection is much greater than that expelled by diffusion. Here, the temperature of the evaporator was considered equal to roughly 25°C (see Ref. [9]). Stated that, the results of the simplified analytical formulation are reported in Fig. 4, together with numerical results obtained considering q_{in} equal to 1000 W m^{-2} and s equal to 1 mm, without losing generality. The black dashed line was obtained by the simplified time-dependent expression reported in Eq. (18), where the Neumann boundary condition ($\frac{\partial a}{\partial \tilde{x}}\big|_{\tilde{x}=1} = 0$) at the axis of symmetry of the device (namely right side in Fig. 1) is verified. This transient analytical solution of the approximate differential equation (Eq. (14)) does not depend on the dimensionless coordinate because the diffusive part of the equation is neglected. Thus, it appears as a simple horizontal line, which varies with time. The comparison between Eq. (18) and the numerical model shows that the approximate solution differs from that obtained numerically, particularly in the vicinity of the Dirichlet condition. It is interesting to note that, away from this, the temporal evolution of the salt concentration described by the simplified model (Eq. (18)) and the number model substantially match for the critical point, which is also the one of major interest for sizing the device to avoid sedimentation and crystallisation phenomena. At the most critical point of the device, namely $\tilde{x} = 1$, the numerical solution aligns closely with the analytical model, deviating by less than 1% only when higher concentrations are reached, close to 350 g L^{-1}. However, it is important to note that any discrepancy should be conservative in nature, with the analytical model typically predicting a greater salt accumulation compared to the numerical model. In the design salinity range, i.e. between 0 g L^{-1} and around 350 g L^{-1}, it is essentially indifferent to refer to the simplified solution or to the numerical solution to describe the temporal evolution of the salt concentration at the most critical point. Then, the blue dash-

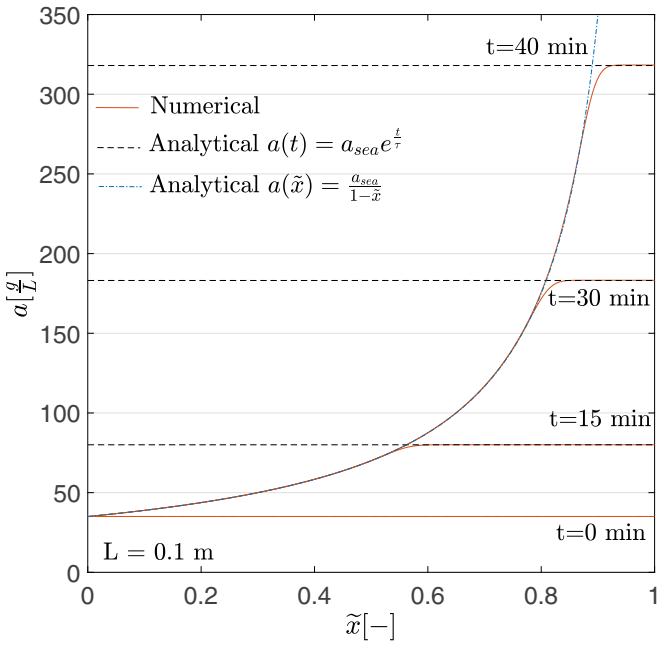

Fig. 4. Time-dependent analytical and numerical results. The salt concentration is reported as function of the dimensionless variable $\tilde{x}$. Red solid line, black dashed line and blue dash-dot line represent the numerical solutions obtained with Eq. (10) and analytical solutions obtained with Eqs. (18) and (21), respectively, being L equal to 0.1 m. Moreover, q_{in} and s are equal to 1000 W m^{-2} and 1 mm, respectively. Solutions for t equal to 0, 15, 30 and 40 min are reported.

dot line was obtained by the steady-state simplified Eq.(21), where the Dirichlet boundary condition is respected. This second analytical solution (Eq. (21)) of the approximate differential equation (Eq. (14)) is not inherently time-dependent. However, it adeptly captures the spatial variation of salt concentration, as dictated by the numerical solution. As time progresses, this correlation grows increasingly accurate, particularly as the system approaches a local steady state. The initial portion of the evaporator, in particular, reaches this equilibrium state before the others.

3.1. Evaluation saturation time

By resorting to the transient simplified model (see Eq. (18)), the time constant Γ of the salt accumulation phenomenon can be identified:

$$a(\tilde{x}, t) = a_{sea}e^{\frac{t}{\Gamma}} \tag{25}$$

where $\Gamma = \frac{1}{k}$. Having fixed the saturation concentration at which salt sedimentation occurs, the saturation time can be evaluated as $t_{sat} = \Gamma \ln \frac{a_{sat}}{a_{sea}}$. Thus, being the solubility of sodium chloride in water equal to $a_{sat} \approx 350$ g L^{-1}, t_{sat} can be evaluated as approximately 2.3 Γ. To have further confirmation of the validity of the simplified model for computing salt saturation times, the latter were calculated with the numerical model (i.e., Eq. (10)) as the main parameters vary. In detail, the numerical saturation time as function of the volumetric absorption of thermal energy $\frac{q_{in}}{s}$ and the length of the wick-based evaporator L, were reported in Fig. 5.

Considering typical and engineering interesting q_{in} and s values (i.e., q_{in} equal to 700 W m^{-2}, which corresponds to the peak value recorded in Turin in August, and s equal to 2 mm), the numerical saturation time ranges from 2.1 and 3.2 h, in case of a L equal to 1 m and 1 cm, respectively. In this scenario, the discrepancy between the saturation time calculated by the numerical and by the simplified analytical approach varies between 4.7% to 37%, in case of a L equal to 1 m and 1 cm, respectively. Moreover, the analytical result always underestimates the more realistic numerical saturation time, resulting in being both a streamlined and a conservative approach. To further assess the validity of Eq. (18), we then considered the experimental results reported in Ref. [22]. To the best of our knowledge, among all the solutions reported in the literature, the one proposed by Zhang and co-workers [22] actually represents the case study most comparable to the one discussed here (in terms of arrangements of the feeding channels and thus physical boundary conditions), wherein a quantitative evaluation of the time-dependent local salt concentration is reported. Therefore, the values of porosity, thickness of the water evaporating layer, evaporation rate and length of the evaporator have been extracted from Ref. [22] and incorporated into Eq. (18). Interestingly, in the region of the device most prone to high salt concentrations, which is of significant engineering interest, Eq. (18) shows a discrepancy of approximately 13% with respect to the experimental value reported in the Ref. [22], which is deemed reasonable and remarkably acceptable. In detail, it is worth noting that Eq. (18) overestimates the experimental measurement, thus still proving to be conservative. The limited deviation observed at the most critical point not only underscores the validity of the proposed model, but also the reliability of the streamlined and simplified analytical formulation for quickly assessing the salt concentration at the most critical point, which mostly impacts device design. Based on these outcomes, we note that non-negligible salt concentrations may be reached after standard operating times for the considered application (i.e., on the order of hours). Therefore, if the accumulated salt is not properly disposed of, a gradually more severe and faster sedimentation process occurs. In fact, overnight salt diffusion (in absence of evaporation) is generally not sufficient to adequately clean the evaporator. To maintain the performance of the device nearly stable, an adequate disposal system for the salt accumulated during the day should be proposed in perspective. This goal may be achieved by using alternative evaporator configurations or special active/passive components able to provide accurate flows, as discussed in the following paragraph.

3.2. On the salt rejection: a case study

The salt accumulation issue may be mitigated by establishing a tailored drainage. At steady state and neglecting diffusion, which rep-

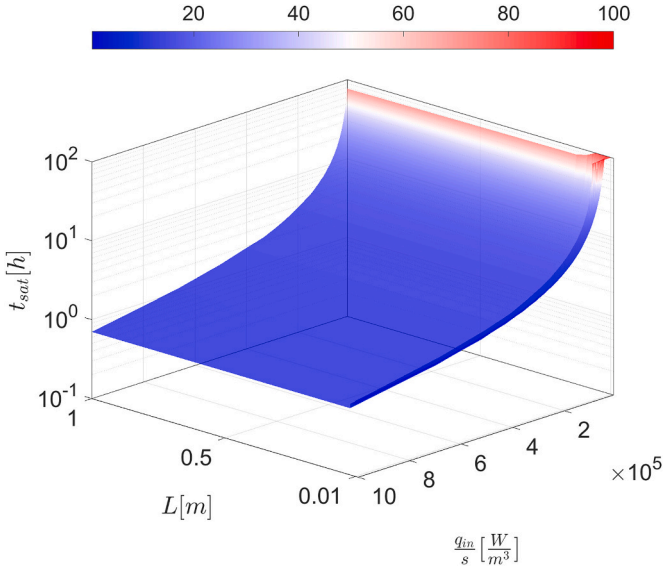

Fig. 5. Numerical saturation time as function of the volumetric absorption of thermal energy $\frac{q_{in}}{s}$ and the length of the wick-based evaporator L. In detail, the following ranges were considered: 100⩽q_{in}⩽10000 W m^{-2}, 1 mm ⩽s⩽1 cm and 1 cm ⩽L ⩽1 m.

resents a conservative assumption since diffusion tends to smooth out any peaks in the salt distribution and expel salt from the evaporator, we have:

$$0 = -\frac{\partial(\dot{m}a)}{\partial\widetilde{x}} \tag{26}$$

where the product $\dot{m}(\widetilde{x})a(\widetilde{x})$ is constant. So, taking into account the specific flow rate trends derived in the previous paragraphs, we get:

$$\dot{m}(\widetilde{x}) = \dot{m}_{\widetilde{x}=0} - \alpha L\widetilde{x} \tag{27}$$

$$a(\widetilde{x}) = \frac{\dot{m}_{\widetilde{x}=0}a_{sea}}{\dot{m}_{\widetilde{x}=0} - \alpha L\widetilde{x}} \tag{28}$$

Then, considering the maximum salinity (i.e., namely $a_{\widetilde{x}=1}$) and the right end of the device (i.e., $\widetilde{x} = 1$; see Fig. 1) as outlet section used for draining, we can get after manipulation the following equation:

$$a(\widetilde{x}=1) = \frac{a_{sea}}{1 - \frac{1}{\frac{\dot{m}_{\widetilde{x}=1}}{\alpha L}+1}} \tag{29}$$

Finally, relying on the condition $a_{\widetilde{x}=1} \leqslant a_{sat}$, the following conservative criterion is obtained:

$$\dot{m}_{\widetilde{x}=1} \geqslant \left(\frac{1}{1 - \frac{a_{sea}}{a_{sat}}} - 1\right)\alpha L \tag{30}$$

Discharge flow rate can be expressed as a percentage of the specific flow rate at the inlet (i.e., at $\widetilde{x} = 0$) to feed the evaporative flow i.e., αL:

$$\Psi = \frac{\dot{m}_{\widetilde{x}=1}}{\dot{m}_{\widetilde{x}=0,evap}} = \left(\frac{1}{1 - \frac{a_{sea}}{a_{sat}}} - 1\right) \approx 11\% \tag{31}$$

By equipping the system under consideration with active/passive components that can provide a specific flow rate at the inlet that is almost 11% higher than that required to supply only the evaporative flow, the eventual crystallization phenomenon may be mitigated. Low-energy pumps should provide the energy quota for re-circulation of only the exceeding flow rate.

4. Discussions and conclusions

The deployment of devices for passive solar/thermal interfacial evaporation, which is expected to be highly attractive owing to the plethora of applications in water purification and desalination fields, is hindered by two main critical aspects. These issues consist of salt crystallization phenomena and the capillary limit and thus the occurrence of dry-out phenomena, emphasized by the fact that these processes are often designed to be low-energy and therefore passive (i.e., no moving mechanical apparatus). Indeed, such processes are implemented through the use of narrow, porous and hydrophilic matrices, which are commonly characterized by tailored photothermal properties. The aforementioned issues need to be addressed carefully, with the goal of stabilizing productivity over time and aiming to implement more scalable technologies.

Here, a mathematical framework is reported to investigate the time-dependent solute transport equation in porous media constituting the evaporator and explore the limitations of the passive solar/thermal interfacial evaporation process. First, the equation describing the velocity reduction of the propagating front due to the interfacial evaporation is based on the findings of our recent work (see Ref. [9]), where details on the fluid flow in porous and hydrophilic wick-based evaporators for water treatment purposes were reported and discussed. In particular, these findings are used to limit the choice of parameters defining the operating conditions, which indeed need to be realistic and safe from a fluid dynamic standpoint as well, and to simplify the study. Numerical analyses were conducted to investigate the effects of different parameters, such as the absorbed thermal energy, the thickness and the length of the wick-based evaporator, on the time-dependent spatial solute concentration. Then, safely neglecting the diffusive contribution, a simplified analytical approach was proposed to easily describe the time-dependent solute concentration at the most critical point of the evaporator, which is also the one of major engineering interest. Through the simplified approach, the phenomenon of solute accumulation is revealed to exhibit an exponential trend over time, as determined by a time constant Γ. The latter mainly depends on the evaporator thickness and absorbed thermal energy. Interestingly, the saturation times can be easily and compactly estimated as 2.3 Γ, considering sodium chloride as the solute. The derived simplified model also showed good agreement with the numerical results. In detail, the saturation time evaluated with the simplified analytical model was estimated equal to 2 h, in the case of a 2-meter overall length device (i.e., $2L$), which is approximately 5% less than the numerically estimated value. For the sake of completeness, an estimate of the extra flow rate, beyond that used to sustain the evaporative flow, was calculated with the aim of mitigating the salt accumulation phenomenon. This extra flow could be provided by a small recirculation pump powered by renewable energy or by mechanical manual or gravity-driven operation.

Design guidelines on how to properly tailor the device based on the operating conditions were discussed. In perspectives, more extensive and comprehensive multi-scale models should be developed to account for the effect of the pore size and materials. The importance of theoretically and numerically analyzing these phenomena derives also from the current lack of experimental measurements related to a systematic investigation of time-dependent solute transport in porous media. Such measurements, currently, are mostly conducted with non-quantitative (often using image-based methods) and/or destructive techniques, which have serious drawbacks (time-consuming, experiments cannot be repeated with the same sample). Finally, further research should be directed towards optimized materials with anti-fouling properties, paving the way for the design of a new generation of porous materials for passive thermal water treatment processes.

CRediT authorship contribution statement

Roberto Raffaele Meo: Methodology, Software, Formal-analysis, Investigation, Resources, Data-curation, Writing-review-editing. **Marina Provenzano:** Formal-analysis, Investigation, Writing-review-editing. **Matteo Morciano:** Conceptualization, Methodology, Software, Formal-analysis, Investigation, Resources, Data-curation, Writing-original-draft, Writing-review-editing, Visualization, Supervision.

Declaration of Competing Interest

The authors declare that they have no known competing financial interests or personal relationships that could have appeared to influence the work reported in this paper.

Data availability

Data will be made available on request.

Acknowledgments

This work was funded by the European Union Horizon Europe research and innovation programme under grant agreement number 101091915 (acronym “MEloDIZER”). Views and opinions expressed are however those of the author(s) only and do not necessarily reflect those

of the European Union or the European Health and Digital Executive Agency (HADEA). Neither the European Union nor the granting authority can be held responsible for them. M.M. thanks the CleanWaterCenter@PoliTo.

References

[1] P. Tao, G. Ni, C. Song, W. Shang, J. Wu, J. Zhu, G. Chen, T. Deng, Solar-driven interfacial evaporation, Nat. Energy 3 (12) (2018) 1031–1041.
[2] M. Sheng, Y. Yang, X. Bin, S. Zhao, C. Pan, F. Nawaz, W. Que, Recent advanced self-propelling salt-blocking technologies for passive solar-driven interfacial evaporation desalination systems, Nano Energy 89 (2021), 106468.
[3] E. Chiavazzo, M. Morciano, F. Viglino, M. Fasano, P. Asinari, Passive solar high-yield seawater desalination by modular and low-cost distillation, Nat. Sustain. 1 (12) (2018) 763–772.
[4] S. Shoeibi, M. Saemian, H. Kargarsharifabad, S. Hosseinzade, N. Rahbar, M. Khiadani, M.M. Rashidi, A review on evaporation improvement of solar still desalination using porous material, Int. Commun. Heat Mass Transfer 138 (2022), 106387.
[5] M. Grzegorzek, K. Wartalska, B. Kaźmierczak, Review of water treatment methods with a focus on energy consumption, Int. Commun. Heat Mass Transfer 143 (2023), 106674.
[6] Z. Wang, T. Horseman, A.P. Straub, N.Y. Yip, D. Li, M. Elimelech, S. Lin, Pathways and challenges for efficient solar-thermal desalination, in: Sci. Adv., 5, 2019, p. eaax0763..
[7] H. Ghasemi, G. Ni, A.M. Marconnet, J. Loomis, S. Yerci, N. Miljkovic, G. Chen, Solar steam generation by heat localization, Nat. Commun. 5 (1) (2014) 1–7.
[8] E. Chiavazzo, Critical aspects to enable viable solar-driven evaporative technologies for water treatment, Nat. Commun. 13 (1) (2022) 1–4.
[9] R.R. Meo, M. Morciano, Investigating the potentials and limitations of capillary-fed vapor generators: A heat and mass transfer study, Int. Commun. Heat Mass Transfer 137 (2022), 106309.
[10] Y. Zhang, T. Xiong, D.K. Nandakumar, S.C. Tan, Structure architecting for salt-rejecting solar interfacial desalination to achieve high-performance evaporation with in situ energy generation, Adv. Sci. 7 (9) (2020) 1903478.
[11] H. Li, Z. Yan, Y. Li, W. Hong, Latest development in salt removal from solar-driven interfacial saline water evaporators: Advanced strategies and challenges, Water Res. 177 (2020), 115770.
[12] X. Wang, Q. Gan, R. Chen, H. Peng, T. Zhang, M. Ye, Water delivery channel design in solar evaporator for efficient and durable water evaporation with salt rejection, ACS Sustain. Chem. Eng. 8 (21) (2020) 7753–7761.
[13] Y. Zhang, H. Zhang, T. Xiong, H. Qu, J.J. Koh, D.K. Nandakumar, J. Wang, S. C. Tan, Manipulating unidirectional fluid transportation to drive sustainable solar water extraction and brine-drenching induced energy generation, Energy & Environ. Sci. 13 (12) (2020) 4891–4902.
[14] G. Ni, S.H. Zandavi, S.M. Javid, S.V. Boriskina, T.A. Cooper, G. Chen, A salt-rejecting floating solar still for low-cost desalination, Energy & Environ. Sci. 11 (6) (2018) 1510–1519.
[15] M. Morciano, M. Fasano, S.V. Boriskina, E. Chiavazzo, P. Asinari, Solar passive distiller with high productivity and marangoni effect-driven salt rejection, Energy & Environ. Sci. 13 (10) (2020) 3646–3655.
[16] X. Yu, Q. Zhang, X. Liu, N. Xu, L. Zhou, Salt-resistive photothermal materials and microstructures for interfacial solar desalination, Frontiers in Energy Research 9 (2021), 721407.
[17] W. Xu, X. Hu, S. Zhuang, Y. Wang, X. Li, L. Zhou, S. Zhu, J. Zhu, Flexible and salt resistant janus absorbers by electrospinning for stable and efficient solar desalination, Adv. Energy Mater. 8 (14) (2018) 1702884.
[18] S. Gao, X. Dong, J. Huang, J. Dong, F.D. Maggio, S. Wang, F. Guo, T. Zhu, Z. Chen, Y. Lai, Bioinspired soot-deposited janus fabrics for sustainable solar steam generation with salt-rejection, Global Challenges 3 (8) (2019) 1800117.
[19] J. Zeng, Q. Wang, Y. Shi, P. Liu, R. Chen, Osmotic pumping and salt rejection by polyelectrolyte hydrogel for continuous solar desalination, Adv. Energy Mater. 9 (38) (2019) 1900552.
[20] Y. Shi, R. Li, Y. Jin, S. Zhuo, L. Shi, J. Chang, S. Hong, K.-C. Ng, P. Wang, A 3d photothermal structure toward improved energy efficiency in solar steam generation, Joule 2 (6) (2018) 1171–1186.
[21] Y. Shi, C. Zhang, R. Li, S. Zhuo, Y. Jin, L. Shi, S. Hong, J. Chang, C. Ong, P. Wang, Solar evaporator with controlled salt precipitation for zero liquid discharge desalination, Environ. Sci. Technol. 52 (20) (2018) 11822–11830.
[22] Y. Xia, Q. Hou, H. Jubaer, Y. Li, Y. Kang, S. Yuan, H. Liu, M.W. Woo, L. Zhang, L. Gao, et al., Spatially isolating salt crystallisation from water evaporation for continuous solar steam generation and salt harvesting, Energy & Environ. Sci. 12 (6) (2019) 1840–1847.
[23] Y. Wang, J. Hu, L. Yu, X. Wu, Y. Zhang, H. Xu, Recent strategies for constructing efficient interfacial solar evaporation systems, Nano Research Energy 2 (2023), e9120062.
[24] J. Mackie, P. Meares, The diffusion of electrolytes in a cation-exchange resin membrane i. theoretical, Proc. Royal Soc. London. Series A. Math. Phys. Sci. 232 (1191) (1955) 498–509.
[25] J. Mackie, P. Meares, The diffusion of electrolytes in a cation-exchange resin membrane. ii. experimental, Proc. Royal Soc. London. Series A. Math. Phys. Sci. 232 (1191) (1955) 510–518.
[26] W.R. Inc., Mathematica, Version 13.2, champaign, IL, 2022. URL: https://www.wolframalpha.com/.
[27] Q. Huang, C. Du, C. Guo, C. Huang, X. Wang, A high-efficiency salt-rejecting solar evaporator with optimized porous structure for continuous solar desalination, Appl. Therm. Eng. 187 (2021), 116515.